

Scaling Surface Mixing/Mixed Layer Depth under Stabilizing Buoyancy Flux

YUTAKA YOSHIKAWA

Graduate School of Science, Kyoto University, Kitashirakawa, Sakyo, Kyoto, Japan

(Manuscript received 5 September 2013, in final form 20 October 2014)

ABSTRACT

This study concerns the combined effects of Earth's rotation and stabilizing surface buoyancy flux upon the wind-induced turbulent mixing in the surface layer. Two different length scales, the Garwood scale and Zilitinkevich scale, have been proposed for the stabilized mixing layer depth under Earth's rotation. Here, this study analyzes observed mixed layer depth plus surface momentum and buoyancy fluxes obtained from Argo floats and satellites, finding that the Zilitinkevich scale is more suited for observed mixed layer depths than the Garwood scale. Large-eddy simulations (LESs) reproduce this observed feature, except under a weak stabilizing flux where the mixed layer depth could not be identified with the buoyancy threshold method (because of insufficient buoyancy difference across the mixed layer base). LESs, however, show that the mixed layer depth if defined with buoyancy ratio relative to its surface value follows the Zilitinkevich scale even under such a weak stabilizing flux. LESs also show that the mixing layer depth is in good agreement with the Zilitinkevich scale. These findings will contribute to better understanding of the response of stabilized mixing/mixed layer depth to surface forcings and hence better estimation/prediction of several processes related to stabilized mixing/mixed layer depth such as air–sea interaction, subduction of surface mixed layer water, and spring blooming of phytoplankton biomass.

1. Introduction

Surface winds induce turbulent mixing in the surface layer, while the mixing is moderated by Earth's rotation. Stabilizing buoyancy fluxes at the ocean surface further weaken wind-induced mixing and shoal the surface mixing layer. The surface mixed layer, through which surface fluxes have been mixed, is a remnant of this surface mixing layer through which surface fluxes are being actively mixed (e.g., Brainerd and Gregg 1995; de Boyer Montegut et al. 2004). Both the surface mixed and mixing layer depths are a key quantity for several oceanic processes such as air–sea interaction, subduction from the surface layer into greater depths (e.g., Marshall et al. 1993), and spring blooming of phytoplankton biomass (e.g., Sverdrup 1953; Obata et al. 1996); correct understandings of dependence of the mixing/mixed layer depth on winds and stabilizing buoyancy flux under Earth's rotation or a scaling law of stabilized mixing/mixed layer depth are crucially important.

The depth of the wind-induced mixing layer in a neutrally stratified rotating fluid is given by the turbulent Ekman layer depth (Rossby and Montgomery 1935) and is derived as follows: surface wind stress (momentum flux) tends to form the logarithmic boundary layer under the ocean surface where the mean velocity shear is given by $U_*/\kappa z$ and eddy viscosity is $\kappa U_* z$. (U_* , κ , and z are the friction velocity, the von Kármán constant, and the distance from the boundary, respectively.) Earth's rotation, however, changes the mean velocity shear from logarithmic and suppresses wind-induced turbulence. Given the eddy viscosity coefficient K_M , the Ekman balance equation (Ekman 1905) gives the turbulent Ekman layer depth as

$$L = \left(\frac{K_M}{|f|} \right)^{1/2}, \quad (1)$$

where f is the Coriolis parameter. Assuming $K_M \sim \kappa U_* L$ as in the logarithmic boundary layer and inserting it in the above equation, the depth scale of the turbulent Ekman boundary layer

$$L_{\text{EKD}} = \kappa \frac{U_*}{|f|} \quad (2)$$

Corresponding author address: Yutaka Yoshikawa, Graduate School of Science, Kyoto University, Kitashirakawa, Sakyo, Kyoto, 606-8502, Japan.
E-mail: yosikawa@kugi.kyoto-u.ac.jp

is obtained (Rossby and Montgomery 1935). This scaling is consistent with recent numerical simulations of the wind-driven flow in neutrally stratified rotating fluid (Zikanov et al. 2003). The simulation showed that the logarithmic boundary layer is limited to within $0.1U_*/|f|$ from the surface. Below that layer, the Ekman boundary layer forms in which eddy viscosity decreases with depth. Such profiles of decreasing eddy viscosity have been observed by field measurements (Chereskin 1995; Yoshikawa et al. 2007, 2010).

The Monin–Obukhov length L_{MOL} (Monin and Obukhov 1954) on the other hand gives a scale of the mixing layer under the stabilizing surface flux. This scale can be derived from a balance between the shear production rate in the logarithmic layer ($U_*^3/\kappa z$) and buoyancy consumption rate B of turbulent kinetic energy (Kundu et al. 2004),

$$L_{\text{MOL}} = -\frac{U_*^3}{\kappa B}, \quad (3)$$

or from the vertically integrated turbulent kinetic energy (TKE) balance equation [shear production (U_*^3) + buoyancy consumption ($BL/2$) = dissipation, where the dissipation is assumed to be proportional to U_*^3]. Though this scale was used as the stabilized mixing (or mixed) layer depth in some previous studies (Kraus and Turner 1967; Qiu and Kelly 1993), lack of Earth's rotation effect in the scale is crucial for estimating that depth, and this resulted in nonnegligible differences between estimations and observations (Garwood 1977; Garwood et al. 1985; Gaspar 1988). This means that both the effects of Earth's rotation and surface stabilizing flux need to be considered simultaneously. A question is how these two effects cooperate or compete with each other to shoal the mixing layer.

Garwood (1977) improved the Monin–Obukhov (or Kraus–Turner) scale by assuming dissipation in the integrated TKE balance equation to be proportional to $U_*^2 f L$ rather than U_*^3 , resulting in

$$L_{\text{G77}} \left(\propto \frac{U_*^3}{U_*^2 f - B} \right) = \frac{1}{a_{\text{G77}}/L_{\text{EKD}} + b_{\text{G77}}/L_{\text{MOL}}}, \quad (4)$$

where a_{G77} and b_{G77} are empirical constants. Gaspar (1988) examined the mixed layer depth observed at the ocean weather station Papa and found that this scale well explains the observed variations of the mixed layer depth. On the other hand, an atmospheric counterpart of stabilized mixing/mixed layer depth is the stably stratified Ekman boundary layer depth, and its scaling was proposed as follows. Assuming $K_M \sim \kappa U_* L_{\text{MOL}}$

under the stabilizing buoyancy flux and inserting it in Eq. (1), the following length scale is obtained (Zilitinkevich 1972):

$$L_{\text{Z72}} = L_{\text{EKD}}^{1/2} L_{\text{MOL}}^{1/2}. \quad (5)$$

Recent large-eddy simulations (LESs) of Goh and Noh (2013) showed the validity of this scale as the oceanic mixed layer depth. Zilitinkevich et al. (2002) further extended this scale to neutral conditions by assuming that the actual stabilized Ekman depth will be more affected by the smaller length scale between L_{EKD} and L_{Z72} as

$$\frac{1}{L^n} = \frac{a}{L_{\text{EKD}}^n} + \frac{b}{L_{\text{Z72}}^n}, \quad (6)$$

where a , b , and n are empirical constants. From observations at three different field experimental sites (Zilitinkevich et al. 2002) and large-eddy simulations (Zilitinkevich et al. 2007) for the atmospheric boundary layer, $n = 2$ is found so that

$$L_{\text{Z02}} = \frac{1}{\sqrt{a_{\text{Z02}}/L_{\text{EKD}}^2 + b_{\text{Z02}}/L_{\text{Z72}}^2}}, \quad (7)$$

where a_{Z02} and b_{Z02} are optimized constants for L_{Z02} . The quantity L_{Z02} is expected to be better than L_{Z72} even for the oceanic surface mixing/mixed layer depth in that it covers the depths under the weak stabilizing buoyancy fluxes where Earth's rotation effect plays more important roles. Applicability of this scaling to the oceanic boundary layer is suggested by Zilitinkevich et al. (2002), though it is not yet validated from observed data.

As described above, two different scales, L_{G77} and L_{Z02} , have been proposed for stabilized mixing layer depth. Though previous studies tested the validity of these scales using the observed mixed layer depth, the number of observations was limited in both the ocean and atmosphere. [The number of ocean stations that can provide detailed time series of the mixed layer depth and atmospheric forcings are few, while the stable atmospheric boundary layer is limited at higher latitudes or at night (short lived) and hence the number of atmospheric observations is also small.] Though previous LES (Goh and Noh 2013) showed good agreement between the mixed layer depth and L_{Z72} in their idealized simulations, agreement with L_{Z02} remains unknown. Differences between the mixed layer depth and the mixing layer depth in ocean surface boundary layer also need to be examined. Thus, further extensive and quantitative examination is required to identify an exact scaling of the mixing/mixed layer depth.

Recent development of Argo float profilers, along with satellite remote sensing, enable us to investigate the scaling of the mixed layer depth in global oceans in an extensive and quantitative manner. In this study, we first analyzed observed oceanic data and investigated parameter dependences of the stabilized mixed layer depth (hereinafter referred to as SMedLD). We assumed that horizontal advection is weak and SMedLD is determined by one-dimensional processes. Only the “shoaling” mixed layer is analyzed to minimize effects of preexisting stratification (that were not examined because of the lack of a global dataset of the stratification). Under these assumptions, relevant external parameters are U_* , f , and $B(<0)$, and the unique nondimensional parameter representing the stabilizing flux effects is $Z = -B/|f|U_*^2 (=L_{\text{EKD}}/\kappa^2 L_{\text{MOL}} = L_{\text{EKD}}^2/\kappa^2 L_{\text{Z72}}^2)$ (Zilitinkevich 1972). The stabilizing flux changes the mixing layer depth scale from L_{EKD} in neutral stratification to $L_{\text{EKD}}F(Z)^{-1}$ in stable stratification, where $F(Z)$ is a nondimensional function of Z representing the stabilizing effect. Note that $F(Z) = 1$, $F(Z) = \kappa^2 Z$, $F(Z) = a + bZ$, and $F(Z) = (a + bZ)^{1/2}$ correspond, respectively, to Eqs. (2) (Ekman scale), (3) (Monin–Obukhov scale), (4) (Garwood scale), and (7) (Zilitinkevich scale). Using observed data described in section 2, we examine the functional form of $F(Z)$ with respect to Z and determine the SMedLD scale (section 3). Global distributions and temporal variations of SMedLD are also shown in that section. In section 4, the validity of the scaling was examined using LESSs. Results of LESSs were also used to discuss differences between SMedLD and the stabilized mixing layer depth (hereafter referred to as SMingLD). Concluding remarks are given in section 5.

2. Data and analytical method

Observed data in the present study are the mixed layer Argo dataset, gridpoint value (MILA-GPV) (Hosoda et al. 2010), satellite-derived surface momentum and heat fluxes of the Japanese Ocean Flux Datasets with Use of Remote Sensing Observations (J-OFURO2) (Kubota et al. 2002; Kutsuwada et al. 2009; Tomita et al. 2010), and satellite-derived surface water flux of the Hamburg Ocean Atmosphere Parameters and Fluxes from Satellite Data (HOAPS) (Fennig et al. 2012). For the MILA-GPV dataset, 10 daily data were downloaded from its website (JAMSTEC 2013). From vertical profiles of potential temperature and density with a 1-m depth interval, mixed layer depth was defined as the shallower among depths determined with $\Delta\sigma_\theta = 0.03 \text{ kg m}^{-3}$ and $\Delta T = 0.2^\circ\text{C}$, where $\Delta\sigma_\theta$ and ΔT are potential density and potential temperature differences between 10-m depth and that depth, respectively. (Because of this definition, the mixed

layer depths defined in this dataset are always greater than 10 m.) Hereinafter, this observed mixed layer depth is denoted as L_{MLD} .

Daily data of momentum and heat fluxes are downloaded from the J-OFURO2 website (J-OFURO Team 2013), while 6-hourly data of surface water flux are downloaded from the HOAPS website (HOAPS Group 2013). Wind stress τ was converted to the (waterside) friction velocity $U_* = (\tau/\rho)^{1/2}$, where ρ (1020 kg m^{-3}) is water density. Net heat flux H and freshwater flux $(E - P)$ were converted to buoyancy flux through $B = -g[\alpha H/C_a \rho - \beta(E - P)S]$, where g ($=9.80 \text{ m s}^{-2}$) is the gravity acceleration, C_a ($=3.90 \times 10^3 \text{ J kg}^{-1} \text{ K}^{-1}$) is the heat capacity of seawater, S is the mixed layer salinity, and α and β are the thermal expansion and haline contraction rates of seawater, respectively. The thermal expansion and haline contraction rates were calculated with the equation of state for seawater (Jackett and McDougall 2006), using the mixed layer temperature and salinity of the MILA-GPV dataset.

The friction velocity and buoyancy fluxes are averaged onto a $2^\circ \times 2^\circ$ grid over 10 days in order to match horizontal and temporal resolutions of surface fluxes with that of the mixed layer data. Figure 1 shows the time series of zonally averaged U_* , B , and L_{MLD} . In later spring (defined here as April–June in the Northern Hemisphere and October–December in the Southern Hemisphere), U_* becomes weaker, B becomes more stabilizing, and hence L_{MLD} becomes smaller (shoaling).

To investigate SMedLD, we selected L_{MLD} that satisfies the following conditions:

- 1) $B \leq B_{\text{thr}}(<0)$ or $H \leq H_{\text{thr}}(<0)$,
- 2) $\partial L_{\text{MLD}}/\partial t < 0$,
- 3) $\partial U_*/\partial t < 0$,
- 4) $\partial B/\partial t < 0$, and
- 5) L_{MLD} in the later spring,

where U_* and B (H) are 10 daily fluxes at the corresponding time and location of (10 daily) L_{MLD} considered, and the time differential was taken between the 10 daily data. The first condition was to discard L_{MLD} under too small B or H . Because such weak forcings generate small buoyancy/temperature difference at the mixed layer base, L_{MLD} (if defined in the dataset) is likely determined by other processes than surface forcings. The threshold values of B_{thr} and H_{thr} above were calculated as follows: A surface buoyancy flux B (<0) during $T_{10} = 10$ days (data interval) induces buoyancy increase $-BT_{10}$ per unit surface area. Because this buoyancy increase is vertically mixed in the mixed layer, the buoyancy increase at each level can be roughly represented as $-BT_{10}/L_{\text{MLD}}$. In order for this mixed layer to be detected in the MILA-GPV dataset, the

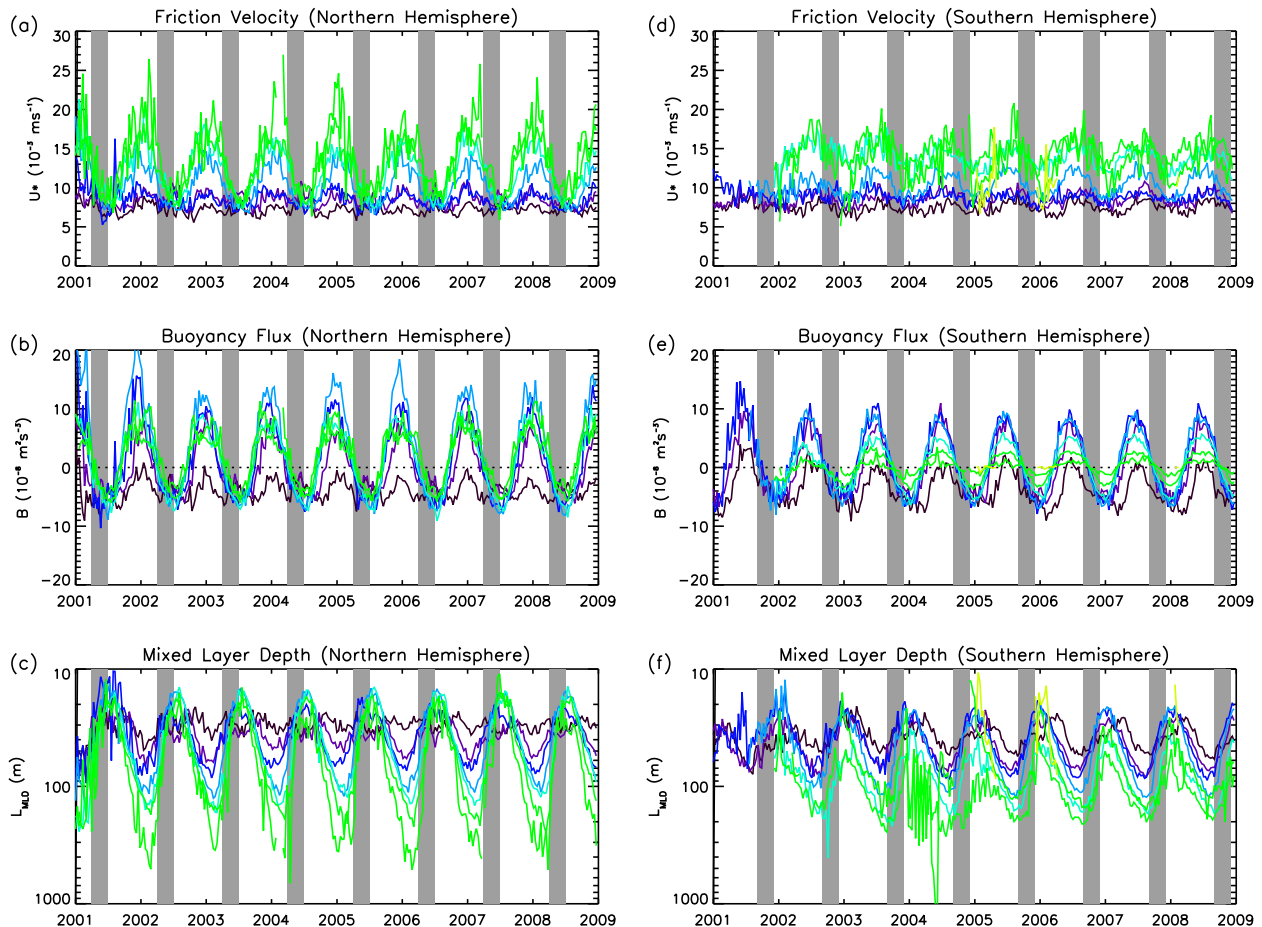


FIG. 1. Time series of zonally averaged (a),(d) U_* , (b),(e) B , and (c),(f) L_{MLD} in the (left) Northern and (right) Southern Hemispheres. Color represents latitudes. (Color legends are in Fig. 2.) Gray hatched area indicates the later spring: April–June (October–November) in the Northern (Southern) Hemisphere.

buoyancy increase at the mixed layer base should be larger than a buoyancy threshold $\Delta b = g\Delta\sigma/\rho$, where $\Delta\sigma$ is the density threshold value (0.03 kg m^{-3}) used in MILA-GPV. Thus, we set $B_{thr} = -g\Delta\sigma/\rho L_{MLD}/T_{10}$. Similarly, H_{thr} was determined from the temperature threshold of MILA-GPV ($\Delta T = 0.2^\circ\text{C}$). The second condition was to exclude other effects than surface forcings (e.g., horizontal advection effects) that might deepen L_{MLD} despite ongoing stabilizing buoyancy flux. Thus, L_{MLD} that shoaled over 10 days was analyzed. However, L_{MLD} sometimes becomes smaller (shoaling) even when surface forcings do not favor it, again because of other processes than surface forcings. To exclude these effects, third and fourth conditions were applied. Finally, L_{MLD} in the later spring was selected in order to reduce contaminations from the other processes. Note, however, that the present results do not largely change even if data in other seasons were included in the following analysis because shoaling of the mixed layer

occasionally occurs even in other seasons because of the short-term variations in surface forcings.

Data at lower latitudes than 2° (equatorial region) were discarded because of longer inertial periods (response time) than 10 days (forcing period). At higher latitudes than 2° , response time of SMedLD to surface forcings will be less than 10 days, and an equilibrium between SMedLD and forcings is expected. The analysis period spans from 2001 to 2008, during which L_{MLD} , U_* , and B were all obtained. The number of matching data of L_{MLD} , U_* , and B is 6759, which is 10.0% of the total data obtained in the later spring.

3. Results

Figure 2 shows $F(Z) = \kappa U_*/|f|L_{MLD}$ as a function of $Z = -B/|f|U_*^2$. A larger Z corresponds to larger stabilizing flux, weaker winds, and lower latitude. These conditions are more typical at lower latitudes. Clearly

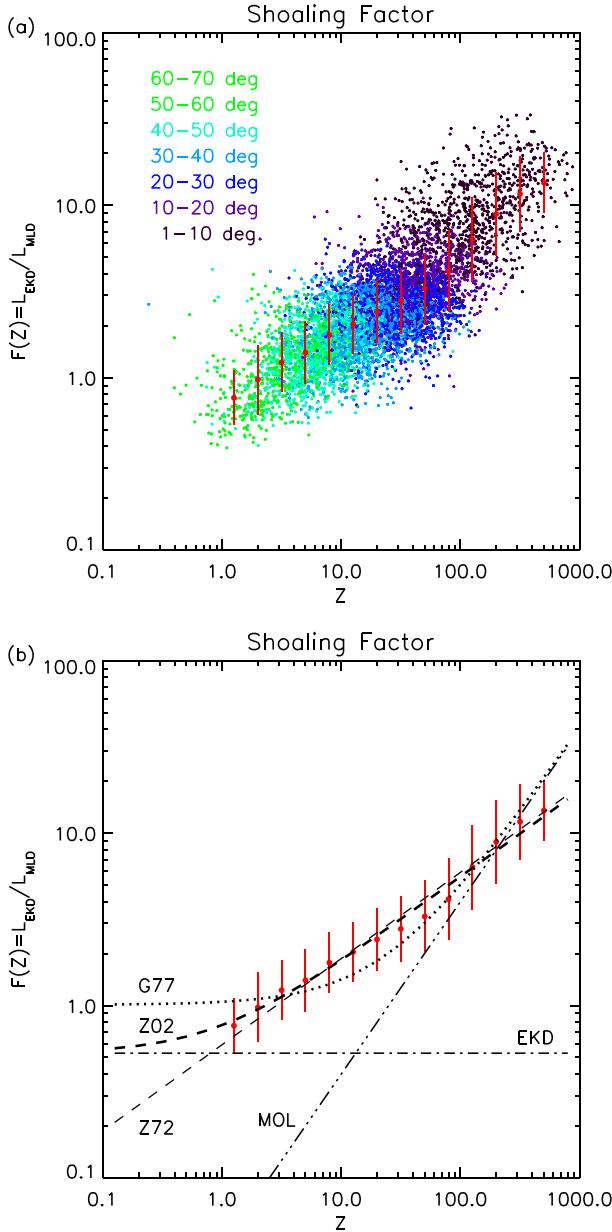


FIG. 2. (a) Scatterplots of $L_{EKD}/L_{MLD} = F(Z)$ as a function of Z . Color of dots represents latitudes. Red circles with vertical bars show average and standard deviation of the observed $F(Z)$. (b) Average and standard deviation of the observed $F(Z)$ along with $F(Z)$ derived from Zilitinkevich et al. (2002) scale (dashed line), Zilitinkevich (1972) scale (thin dashed line), Garwood scale (dotted line), Monin–Obukhov scale (dash three dotted line), and Ekman scale (dashed–dotted line).

$F(Z)$ increases with Z , indicating that SMedLD becomes shallower as Z (normalized stabilizing flux) increases. In the figure, mean and standard deviations of $F(Z)$ at each $\log_{10}Z$ interval were overplotted. Though scatter is large, significant dependence of $F(Z)$ on Z is clearly

found. This indicates that one-dimensional processes capture a significant fraction of the variability.

In the figure, $F(Z)$ corresponding to Ekman, Monin–Obukhov, Garwood, and Zilitinkevich scales are overplotted. Coefficients in L_{Z02} ($a_{Z02} = 0.28$ and $b_{Z02} = 0.31$) and L_{G77} ($a_{G77} = 1.01$ and $b_{G77} = 0.04$) were determined respectively by matching each $F(Z)$ with the observed $F(Z)$ in a least squares sense. In this figure, a_{Z02} and b_{G77} are used in $F(Z)$ of Ekman and Monin–Obukhov scales, respectively. The Zilitinkevich scale L_{Z02} is found to be the best among these scales in following the observed $F(Z)$ over $1.0 \leq Z \leq 500$. Note that $F(Z) = (0.35Z)^{1/2}$, corresponding to L_{Z72} also explains well the observed $F(Z)$. Because of slight differences between L_{Z02} and L_{Z72} over the observed range of Z , whether L_{Z02} is better than L_{Z72} remains unclear from this analysis. [One might think that L_{Z02} never scale L_{MLD} at smaller Z or $|B|$ because L_{MLD} defined with a certain threshold value (Δb) becomes infinitely large as B goes to zero. However, in principal, L_{Z02} can scale L_{MLD} if B continues for long period (T) so that BT remains finitely large or if L_{MLD} was defined alternatively, as described in the next section.] Of importance here is that $F(Z) \propto Z^{1/2}$ (part of the Zilitinkevich scale) captures SMedLD response to stabilizing surface forcings for $Z \geq 2$, while the Garwood scale (as well as Ekman and Monin–Obukhov scales) fails to explain it. This is consistent with recent field experiments in the atmospheric boundary layer (Zilitinkevich et al. 2002) and recent LESs for the atmospheric (Zilitinkevich et al. 2007) and oceanic (Goh and Noh 2013) stable boundary layers. In the following, L_{Z02} is used as the Zilitinkevich scale because L_{Z02} is almost the same with (or slightly better than) L_{Z72} for $Z > 2$.

Figure 3 compares L_{MLD} with L_{Z02} , L_{G77} , and L_{MOL} . Though scatter is large in all cases, the slope of the regression line (1.03), correlation coefficient (0.59), and root-mean-square difference (0.19) are better for L_{Z02} than L_{G77} . Apparently, L_{MOL} overestimates (underestimates) L_{MLD} at higher (lower) latitudes. This demonstrates that use of L_{MOL} (or the Kraus–Turner model) over wide meridional range is not appropriate.

Global distributions of L_{MLD} , L_{G77} , and L_{Z02} are shown in Fig. 4. These maps are obtained by averaging respective quantities in each grid cell. On these maps, depths averaged over April–June (October–December) are plotted in the Northern (Southern) Hemisphere. The observed SMedLD (L_{MLD}) is typically less than a few tens of meters, except for the central subtropical Pacific and Atlantic Oceans and higher latitudes than 45° (Fig. 4a). The greatest SMedLD exceeds 100 m and is found in the Antarctic Circumpolar Current (ACC) region. It is again clear that L_{Z02} successfully captures

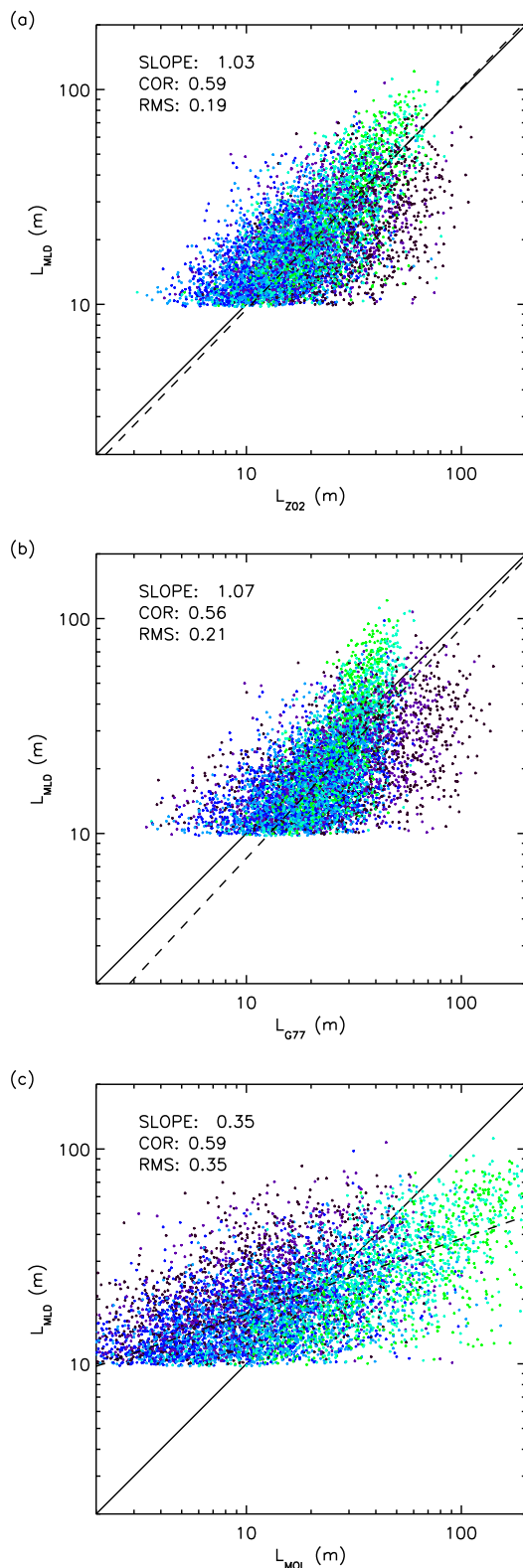


FIG. 3. Scatterplots of the relationship between L_{MLD} and (a) L_{Z02} , (b) L_{G77} , and (c) L_{MOL} . Dashed line shows regression line. Color of dots represents latitudes, as in Fig. 2.

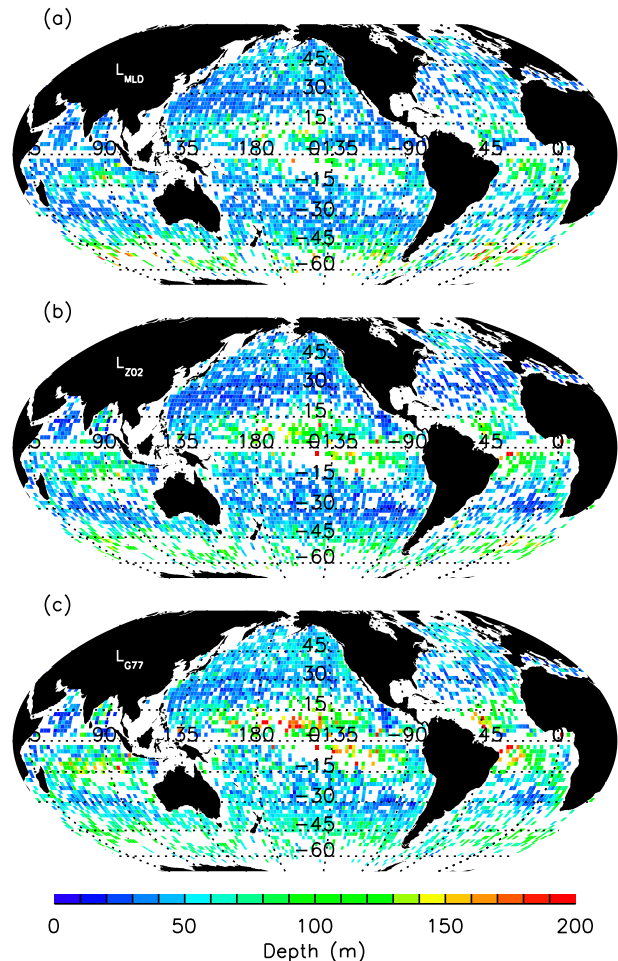


FIG. 4. Global distribution of (a) L_{MLD} , (b) L_{Z02} , and (c) L_{G77} . White areas show regions of missing or discarded data (section 2).

global distribution of L_{MLD} , while L_{G77} overestimated SMedLD in the central subtropical Pacific and Atlantic, where $10 \leq Z \leq 40$ and a systematic difference between L_{MLD} and L_{G77} is found (Fig. 2).

Contributions of wind mixing and buoyancy stabilization to L_{Z02} (and hence L_{MLD}) may be understood by decomposing L_{Z02} into $L_{EKD}/F(0)$ (optimized Ekman depth) and $F(Z)/F(0)$ (referred to as the shoaling factor). The wind mixing tends to make SMedLD greater than 150 m at latitudes lower than 15° (not shown), but the shoaling factor, which is also large at lower latitudes (Fig. 5a), prevents such greater SMedLD. In the central subtropical Pacific and Atlantic Oceans, where SMedLD is relatively larger, momentum fluxes are larger (Fig. 5b), while buoyancy fluxes are smaller (Fig. 5c), resulting in smaller Z (nondimensional buoyancy-stabilization effect) and hence the smaller shoaling factor (Fig. 5a) and greater SMedLD. On the other hand, at higher latitudes (e.g., higher than 45°), the shoaling factor is close

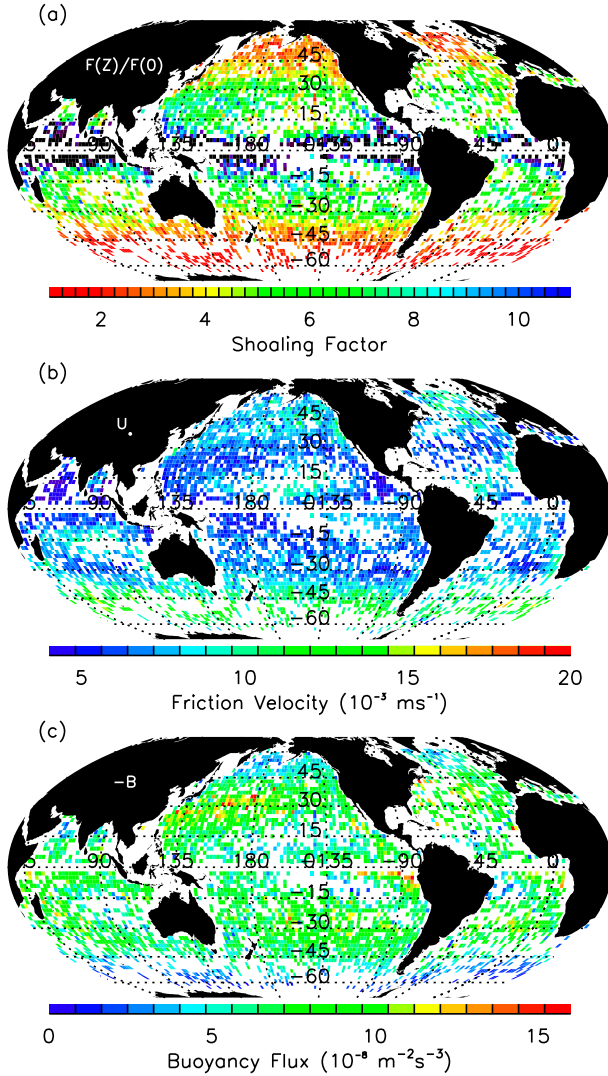


FIG. 5. As in Fig. 4, but for (a) $F(Z)/F(0)$, (b) U_* , and (c) $-B$.

to its lowest value because of greater friction velocity, smaller stabilizing buoyancy flux, and larger $|f|$. Note that $F(Z)/F(0)$ is smaller at 45°S than at 30°S , though B is similar at these latitudes. This demonstrates that stabilization effects cannot be quantified without U_* and f .

Figure 6 shows temporal variations of zonally averaged L_{MLD} and L_{Z02} . Note again that L_{MLD} and L_{Z02} from April to June (from October to December) are plotted in the northern (southern) half area of the figure. Temporal variations in L_{MLD} (Fig. 6a) are well followed by those in L_{Z02} (Fig. 6b), though their difference is systematically large at lower latitudes than 10° (Fig. 6c). Other processes not considered in the present analysis (such as Ekman pumping) may be responsible for this difference as discussed in section 5.

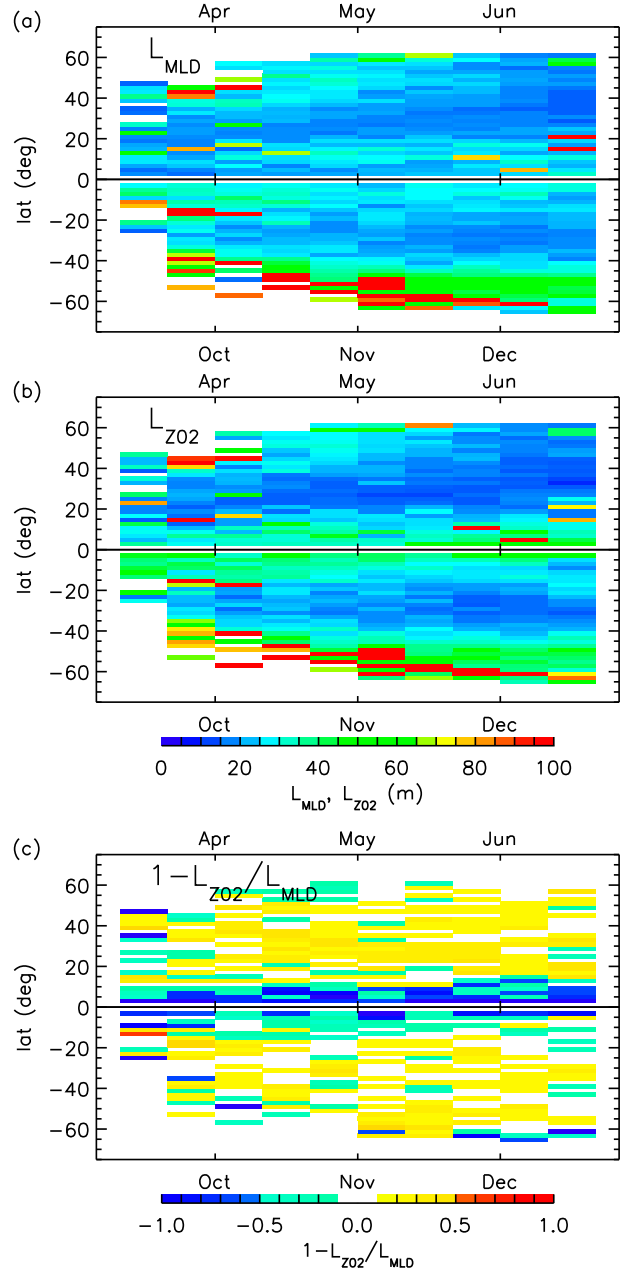


FIG. 6. Monthly variations of zonally averaged (a) L_{MLD} , (b) L_{Z02} , and (c) $1 - L_{\text{Z02}}/L_{\text{MLD}}$ from April to June (from October to December) in the Northern (Southern) Hemisphere. Note that deviations greater than $\pm 50\%$ [blue and red colors in (c)] corresponds roughly to $10^{\pm \text{RMS}}$ with $\text{RMS} = 0.19$ (Fig. 3b).

4. Validation with LESS

Though good agreement between observed L_{MLD} and the Zilitinkevich scale (L_{Z02} or L_{Z72}) was found in observed data, further validation of this agreement will be required because of the large scatter between them (Figs. 2, 3). Effects of the diurnal cycle

TABLE 1. LES parameters (climatological forcing case).

Lat (°)	$f (\times 10^{-4} \text{ s}^{-1})$	$U_* (\times 10^{-3} \text{ m s}^{-1})$	$B_{\text{AV}} (\times 10^{-8} \text{ m}^2 \text{ s}^{-3})$	$H_{\text{DC}} (\text{W m}^{-2})$	$D (\text{m})$	Z
−63.0	−1.30	9.99	0.659	120	155.0	0.510
−61.0	−1.27	10.7	1.10	120	160.0	0.755
−59.0	−1.25	12.1	2.49	180	163.0	1.36
−47.0	−1.06	12.1	4.08	210	159.0	2.62
−43.0	−0.992	10.7	4.65	210	129.0	4.09
−39.0	−0.915	9.19	5.37	250	97.9	6.95
−31.0	−0.749	7.37	5.94	250	69.4	14.6
−11.0	−0.278	8.06	4.83	250	155.0	26.8
−7.0	−0.177	7.56	5.18	240	166.0	51.1
−3.0	−0.0761	6.56	7.49	240	161.0	229.0

of the surface heat flux on L_{MLD} need also be examined because these effects are usually large in the oceanic surface boundary layer, but not considered in the original Zilitinkevich scale. In this section, large-eddy simulations were performed for this purpose.

a. Model configuration

Governing equations are the momentum equations, continuity equation, and advection–diffusion equation of buoyancy under the incompressible, f -plane,

rigid-lid, and Boussinesq approximations. The model is basically similar to our previous nonhydrostatic model (Yoshikawa et al. 2001, 2012), except for increased grid resolution and use of subgrid-scale parameterization of Deardorff (1980), in order for turbulent flows to be resolved.

The model ocean in this study was horizontally uniform. A constant momentum flux (U_*^2) and a diurnally cycling surface buoyancy flux $B(t)$ were imposed at the surface, while flux-free conditions were used at the bottom. Here, $B(t)$ over 1 day was given by

$$B(t) = B_{\text{AV}} + \begin{cases} -B_{\text{DC}}/\pi & 0 \leq t < T_1/2 \\ -\pi B_{\text{DC}} \sin(2\pi t/T_1) - B_{\text{DC}}/\pi & T_1/2 \leq t < T_1 \end{cases},$$

where $T_1 = 1$ day, B_{AV} is the daily averaged value of $B(t)$, and B_{DC} represents the magnitude of the diurnal cycling component. Thus, the surface was steadily destabilized (cooled) in the first half of each day, while it was stabilized (heated) in a sinusoidal manner in the second half. This cycle was repeated daily over the integration period. For U_* and B_{AV} , zonally averaged U_* and B in the later spring shown in Fig. 1 were used. Zonally averaged National Centers for Environmental Prediction (NCEP)–National Center for Atmospheric Research (NCAR) climatology of downward short-wave radiation (H_{DC}) shown in Hatzianastassiou and Vardavas (2001) was used to calculate $B_{\text{DC}} (= g\alpha H_{\text{DC}}/C_a\rho)$, where α was set as constant ($2.55 \times 10^{-4} \text{ K}^{-1}$).

Model domain was set as cubic ($D \times D \times D$ dimensions) with periodic side boundaries. The model dimension D was set as $4 \times L_{\text{Z02}}$, where $L_{\text{Z02}} = U_*/f(0.3 + 0.3Z)^{1/2}$ with $Z = -B_{\text{AV}}/|f|U_*^2$.

The governing equations and boundary conditions were approximated by second-order finite difference equations. Time integration was performed using the second-order Runge–Kutta scheme. The number of grid cells was $128 \times 128 \times 128$. The grid spacing was

horizontally uniform while vertically variable, with smaller grid spacing near the surface.

A total of 10 experiments were performed with climatological forcings (Table 1). The Southern Hemisphere was selected because the smallest (0.51) and largest (229) Z were observed there. In all the experiments, the subinertial range of power spectra was identified, indicating that turbulent flows were successfully resolved. The modeled mixed layer depth (denoted hereafter as L_*) was calculated as in the MILA-GPV dataset; L_* is the depth at which the density first exceeds its value at 10-m depth by 0.03 kg m^{-3} . Time integration continued for 10 days (T_{10}), with simulated results being recorded every hour.

b. The “mixed” layer depth

Figure 7 shows temporal variations in the horizontally averaged buoyancy profile in several experiments. In the first half of each day, convection took place to mix the buoyancy in the vertical, while in the second half, buoyancy was stratified in the surface layer. Because net buoyancy flux is downward (stabilizing), surface buoyancy gradually increased with time. The modeled mixed

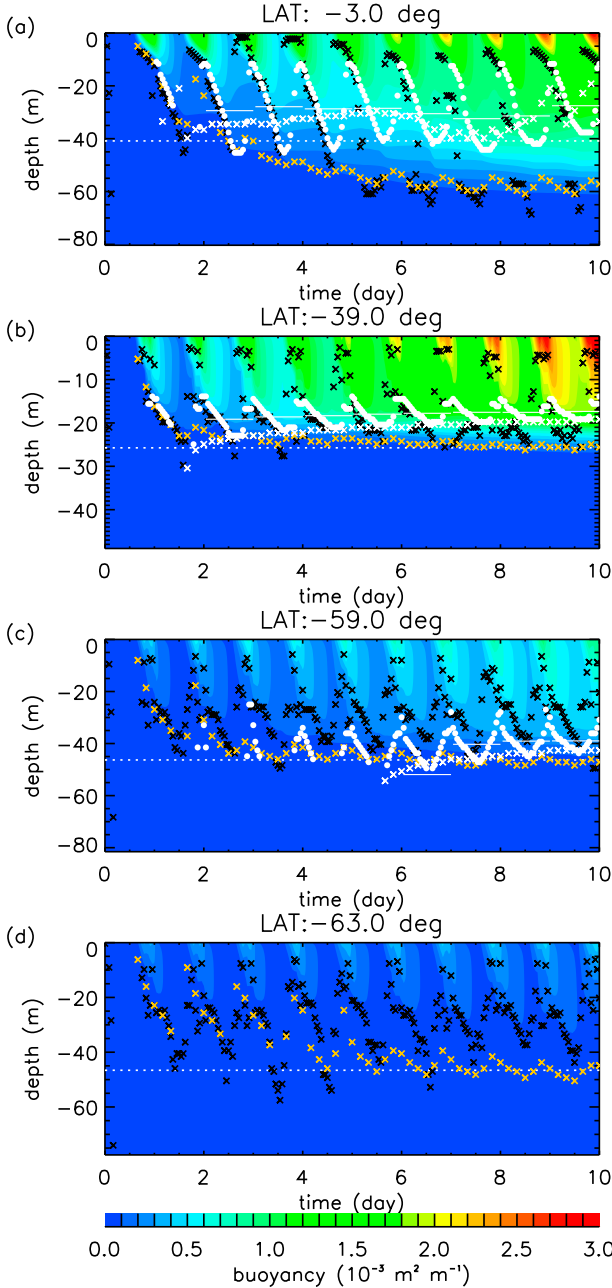


FIG. 7. Temporal variations in buoyancy profile (color) and the mixing/mixed layer depths in LESs. White solid circles show L_* , a counterpart of L_{MLD} (observed mixed layer), simulated under diurnally cycling surface buoyancy flux. Thin white lines show daily average of L_* . White crosses denote L_* under steady surface buoyancy flux. Yellow crosses show L'_* , the mixed layer depth defined with the buoyancy ratio. Black crosses represent L_{**} , the mixing layer depth determined from TKE profile. White dotted lines denote L_{Z02} : (a) 3°S, (b) 39°S, (c) 59°S, and (d) 63°S.

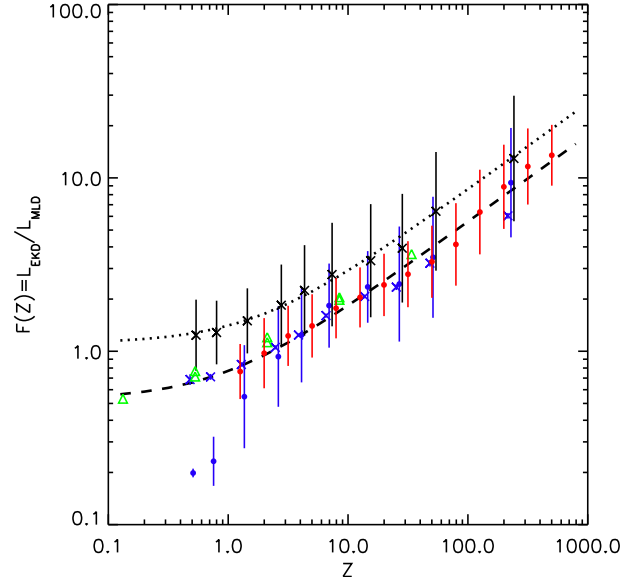


FIG. 8. As in Fig. 2b, but for L_{EKD}/L_* (blue circle), L_{EKD}/L'_* (blue cross), and L_{EKD}/L_{**} (black cross) as well as L_{EKD}/L_{MLD} (red circle). Dashed line shows L_{Z02} optimized for L_{EKD}/L_{MLD} , while the dotted line denotes L_{Z02} optimized for L_{EKD}/L_* . Green triangles show the results of idealized LESs in which the mixed layer depth was defined as the depth of the largest stratification as in Goh and Noh (2013).

layer depth L_* became quasi steady by $t = T_{10}$, except in the experiment at 63°S, where buoyancy increase in the mixed layer was too small and hence L_* could not be defined, though the mixed layer is apparently formed in buoyancy profile (Fig. 7d). The period of this undefined L_* occupies less than 25% over 10 days at lower latitudes than 47°S, but it occupies larger than 40% at higher latitudes than 47°S. Here, L_* was set as $4 L_{Z02}(=D)$ if it could not be defined. Longer periods of undefined L_* results in overestimation of the mixed layer depth as described next.

Average and standard deviation of $F(Z) = L_{EKD}/L_*$ over 10 days ($0 < t \leq T_{10}$) were calculated and plotted along with the observed ones (L_{EKD}/L_{MLD}) in Fig. 8. At $Z > 3$, the averaged L_{EKD}/L_* agrees well with L_{EKD}/L_{MLD} . On the other hand, L_{EKD}/L_* is significantly smaller than L_{EKD}/L_{MLD} (L_* is greater than L_{MLD}) at $Z < 3$ because of the longer period of undefined L_* at higher latitudes where the surface buoyancy flux is weaker (and hence Z is smaller). This suggests that the observed $F(Z) = L_{EKD}/L_{MLD}$ at $Z < 3$ (Fig. 2) might be determined by other processes than 10-daily averaged surface forcings. At $Z > 3$, however, L_{EKD}/L_* agrees well with L_{EKD}/L_{MLD} . Good correspondence between the observed and simulated $F(Z)$ suggests that L_{MLD} actually represents the mixed layer depth determined by stabilizing surface forcings.

TABLE 2. LES parameters (idealized forcing case).

$f(\times 10^{-4} \text{ s}^{-1})$	$U_* (\times 10^{-3} \text{ m s}^{-1})$	$B_{AV} (\times 10^{-8} \text{ m}^2 \text{ s}^{-3})$	$D \text{ (m)}$	Z
1.0	40.0	2.0	400.0	0.125
1.0	40.0	8.0	400.0	0.5
1.0	10.0	2.0	100.0	2.0
1.0	10.0	8.0	100.0	8.0
0.25	40.0	2.0	1600.0	0.5
0.25	40.0	8.0	1600.0	2.0
0.25	10.0	2.0	200.0	8.0
0.25	10.0	8.0	100.0	32.0

The experiment for 63°S shows that L_{MLD} defined with $\Delta\sigma = 0.03 \text{ kg m}^{-3}$ failed to capture the simulated mixed layer, resulting in deviation of L_{EKD}/L_* from the Zilitinkevich scale at $Z < 3$. To avoid this failure, we also defined the mixed layer depth in LESs as the depth of 10% buoyancy relative to its surface value. This alternative mixed layer depth (denoted as L'_*) was successfully defined even at $Z < 3$ and became quasi steady after $t = T_5$ ($=5$ days). In Fig. 8, average and standard deviation of L_{EKD}/L'_* in this quasi-steady period ($T_5 < t < T_{10}$) were also plotted. Good agreement between L_{EKD}/L'_* and L_{MLD}/L_{Z02} is found except in the 3°S experiment ($Z = 228$), demonstrating that L_{Z02} well captures the response of the quasi-steady mixed layer depth to stabilizing surface forcings.

Note that Goh and Noh (2013) reported their mixed layer depth (defined at the depth of the largest stratification) followed L_{Z72} (rather than L_{Z02}) from $Z (= \lambda/L$ in their notation) $= 20$ down to 0.42. To see the validity of L_{Z02} at such smaller Z , LESs from $Z = 32$ to 0.125 were additionally performed with idealized forcings (Table 2). Our LESs show that the mixed layer depth defined as in Goh and Noh (2013) follows L_{Z02} down to $Z = 0.125$ (green triangle in Fig. 8), showing the validity of L_{Z02} rather than L_{Z72} .

Diurnal cycle effects on the mixed layer depth can be examined by performing LESs with $B_{\text{DC}} = 0$ (no diurnal cycle in surface buoyancy flux). Time evolutions of L_* estimated in these LESs were also shown in Fig. 8. Close correspondence between L_* with $B_{\text{DC}} = 0$ and daily averaged L_* with $B_{\text{DC}} \neq 0$ is found, though the former is slightly smaller than the latter. These results suggest that the diurnal cycle in the surface buoyancy flux makes diurnal variations of SMedLD larger, while it does not change dependence of averaged SMedLD on Z .

c. The “mixing” layer depths

Zilitinkevich scale was originally proposed for the mixing layer depth rather than the mixed layer depth. Though the mixing layer depth is hardly estimated from Argo float profiles, it can be easily estimated in LESs.

To see the validity of the Zilitinkevich scale as the SMingLD in the ocean surface boundary layer under diurnally cycling surface buoyancy flux, the response of the simulated mixing layer depth to surface forcings was also examined.

Because the mixing layer is a layer of active mixing (Brainerd and Gregg 1995), it can be defined using TKE $\overline{u'_i u'_i}/2$ (where u'_i denotes velocity anomaly from its horizontal mean $\overline{u_i}$). In this analysis, the mixing layer depth (denoted as L_{**}) was defined as the depth of 10% TKE relative to its surface value.

The mixing layer depth L_{**} estimated every hour is shown in Fig. 7. It shows large diurnal variations as L_* shows. Though L_{**} is occasionally larger than L_* at lower latitudes, the greatest L_{**} in each day agrees well with L'_* (the depth of 10% buoyancy relative to its surface value).

Average and standard deviation of $F(Z) = L_{\text{EKD}}/L_{**}$ over 5 days ($T_5 \leq t \leq T_{10}$) were calculated and plotted in Fig. 8. The averaged $F(Z)$ approaches constant value as Z becomes small, while $F(Z)$ is proportional to $Z^{1/2}$ as Z increases. This feature agrees well with those of the Zilitinkevich scale. Thus, the Zilitinkevich scale captures quasi-steady SMingLD even in the ocean surface layer where the effects of diurnal variations in the surface buoyancy flux are often large.

5. Concluding remarks and discussion

The present analysis of the mixed layer depth L_{MLD} estimated from Argo float profiles and surface wind stress (ρU_*^2) and surface buoyancy flux (B) estimated from satellite showed that L_{MLD} under stabilizing buoyancy flux ($B < 0$) responds to U_* and B in a manner that $L_{\text{MLD}} = U_*/f(0.28 + 0.31Z)^{1/2}$ or $U_*/f(0.35Z)^{1/2}$ at $Z > 2$, where $Z = -B/|f|U_*^2$ is the normalized surface buoyancy flux. Large-eddy simulations (LESs) performed under zonally averaged steady U_* and diurnally cycling B reproduce this feature. This suggests that Zilitinkevich’s scale $L_{Z02} = U_*/f(a + bZ)^{1/2}$ (Zilitinkevich et al. 2002, 2007), originally proposed for stable atmospheric boundary layer, can be used as the stabilized mixed layer depth scale in the ocean surface boundary layer. Our LESs also showed that L_{Z02} can be used as a valid scale of the mixed layer depth scale even at $Z < 2$ if the depth is defined based on the buoyancy ratio rather than buoyancy difference. LESs also showed that the simulated mixing layer depth is well scaled by the Zilitinkevich scale, even under the diurnally cycling surface buoyancy flux that is typical in the ocean surface boundary layer. It was also found that the diurnal cycle in surface buoyancy flux does not change the dependences of the mixing/mixed layer depths on stabilizing surface forcings, though it enlarges its diurnal variations.

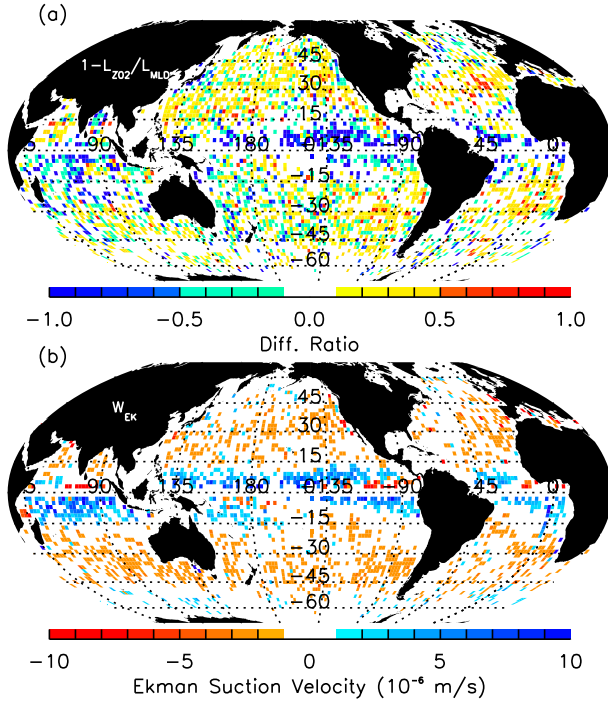


FIG. 9. As in Fig. 4, but for (a) $1 - L_{Z02}/L_{MLD}$ and (b) $\text{curl}\tau/pf$. Note that deviations greater than $\pm 50\%$ [blue and red colors in (a)] correspond roughly to $10^{\pm \text{RMS}}$ with $\text{RMS} = 0.19$ (Fig. 3b).

This scaling enables us to know how the stabilized mixed and mixing layer depths respond to surface momentum and heat fluxes, both of which can be remotely estimated from satellites. This scaling is thus expected to contribute to better estimation/prediction of several processes as mentioned in section 1.

Note that the global distribution of $L_{MLD} - L_{Z02}$ (Fig. 9a) shows that L_{Z02} tends to overestimate L_{MLD} at lower latitudes than 10° . Some other processes not considered in the present study affect the mixing/mixed layer depth. One possible process is Ekman upwelling ($\text{curl}\tau/pf$) that can uplift the mixing/mixed layer base. In fact, the region of large upwellings (Fig. 9b) estimated from the wind stress curl averaged over the period of corresponding L_{MLD} (L_{Z02}) agrees fairly well with the overestimated region (Fig. 9a).

The present study focuses on the mixing/mixed layer depth stabilized by surface buoyancy flux. For this purpose, a large portion of data that are likely affected by other processes such as preexisting stratification (e.g., Pollard et al. 1973; Lozovatsky et al. 2005) were discarded from the present analysis (section 2). Figure 10 shows the $F(Z)$ calculated from all L_{MLD} in the later spring [denoted as $F'(Z)$ and L'_{MLD} , respectively]. Averages of $F'(Z)$ (L'_{MLD}) are larger (smaller) than $F(Z)$ (L_{MLD}) at all Z , probably because preexisting

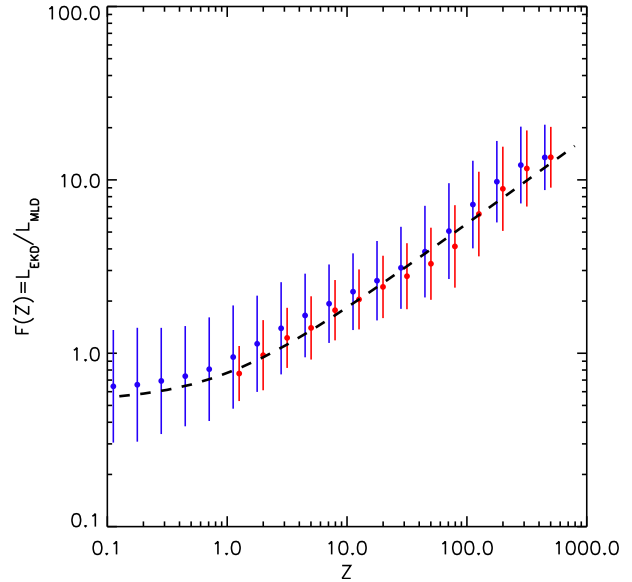


FIG. 10. As in Fig. 2b, but for $F'(Z) = L_{EKD}/L'_{MLD}$ (blue circle and bar), where L'_{MLD} is the mixed layer depth calculated from the all later-spring data. Red circle/bars and black dashed line are the same as those in Fig. 2b.

stratification prevents deepening of the mixing/mixed layer. Standard deviations of $F'(Z)$ are larger than those of $F(Z)$, perhaps because of the advection that can result in shoaling and deepening of the mixing/mixed layer. Interestingly, overall dependence of $F'(Z)$ on Z is similar to the Zilitinkevich scaling. This may indicate that averaged effects of these processes are secondary on global distribution of the mixing/mixed layer depth. Further detailed investigation is necessary for better understanding of these effects, and it will be done in our future study.

Acknowledgments. We express our sincere thanks to Dr. Niino, Dr. Hosoda, and three anonymous reviewers for their instructive comments. Part of this study is supported by JSPS KAKENHI Grant Numbers 22740314 and 25287123 and by the Collaborative Research Program of Research Institute for Applied Mechanics, Kyushu University.

REFERENCES

- Brainerd, K., and M. C. Gregg, 1995: Surface mixed and mixing layer depths. *Deep-Sea Res.*, **42**, 1521–1543, doi:10.1016/0967-0637(95)00068-H.
- Chereskin, T. K., 1995: Direct evidence for an Ekman balance in the California Current. *J. Geophys. Res.*, **100**, 18 261–18 269, doi:10.1029/95JC02182.
- Deardorff, J. W., 1980: Stratocumulus-capped mixed layers derived from a three-dimensional model. *Bound.-Layer Meteor.*, **18**, 495–527, doi:10.1007/BF00119502.

- de Boyer Montegut, C., G. Madec, A. S. Fisher, A. Lazar, and D. Iudicone, 2004: Mixed layer depth over the global ocean: An examination of profile data and a profile-based climatology. *J. Geophys. Res.*, **109**, C12003, doi:10.1029/2004JC002378.
- Ekman, V. W., 1905: On the influence of the earth's rotation on ocean-currents. *Ark. Mat. Astron. Fys.*, **2**, 1–52. [Available online at <https://jscholarship.library.jhu.edu/handle/1774.2/33989>.]
- Fennig, K., A. Andersson, S. Bakan, C. Klepp, and M. Schroeder, 2012: Hamburg Ocean Atmosphere Parameters and Fluxes from Satellite Data—HOAPS 3.2—Monthly means/6-hourly composites. Satellite Application Facility on Climate Monitoring dataset, doi:10.5676/EUM_SAF_CM/HOAPS/V001.
- Garwood, R. W., 1977: An oceanic mixed layer model capable of simulating cyclic states. *J. Phys. Oceanogr.*, **7**, 455–478, doi:10.1175/1520-0485(1977)007<0455:AOMLMC>2.0.CO;2.
- , P. C. Gallacher, and P. Muller, 1985: Wind direction and equilibrium mixed layer depth: General theory. *J. Phys. Oceanogr.*, **15**, 1325–1331, doi:10.1175/1520-0485(1985)015<1325:WDAEML>2.0.CO;2.
- Gaspar, P., 1988: Modeling the seasonal cycle of the upper ocean. *J. Phys. Oceanogr.*, **18**, 161–180, doi:10.1175/1520-0485(1988)018<0161:MTSCOT>2.0.CO;2.
- Goh, G., and Y. Noh, 2013: Influence of the Coriolis force on the formation of a seasonal thermocline. *Ocean Dyn.*, **63**, 1083–1092, doi:10.1007/s10236-013-0645-x.
- Hatzianastassiou, N., and I. Vardavas, 2001: Shortwave radiation budget of the Southern Hemisphere using ISCCP C2 and NCEP–NCAR climatological data. *J. Climate*, **14**, 4319–4329, doi:10.1175/1520-0442(2001)014<4319:SRBOTS>2.0.CO;2.
- HOAPS Group, cited 2013: Hamburg Ocean Atmosphere Parameters and Fluxes from Satellite Data. [Available online at www.hoaps.org/]
- Hosoda, S., T. Ohira, K. Sato, and T. Suga, 2010: Improved description of global mixed-layer depth using Argo profiling floats. *J. Oceanogr.*, **66**, 773–787, doi:10.1007/s10872-010-0063-3.
- Jackett, D. R., and T. J. McDougall, 2006: Algorithms for density, potential temperature, conservative temperature, and the freezing temperature of sea water. *J. Atmos. Oceanic Technol.*, **23**, 1709–1728, doi:10.1175/JTECH1946.1.
- JAMSTEC, cited 2013: Mixed layer data set of Argo, grid point value. [Available online at www.jamstec.go.jp/ARGO/argo_web/MILAGPV/index.html.]
- J-OFURO Team, cited 2013: Japanese ocean flux data sets with use of remote sensing observations. [Available online at <http://dtsv.scc.u-tokai.ac.jp/j-ofuro/>.]
- Kraus, E. B., and J. S. Turner, 1967: A one-dimensional model of the seasonal thermocline II. The general theory and its consequences. *Tellus*, **19**, 98–106, doi:10.1111/j.2153-3490.1967.tb01462.x.
- Kubota, M., N. Iwasaka, S. Kizu, M. Konda, and K. Kutsuwada, 2002: Japanese Ocean Flux Datasets with Use of Remote Sensing Observations (J-OFURO). *J. Oceanogr.*, **58**, 213–225, doi:10.1023/A:1015845321836.
- Kundu, P. K., I. M. Cohen, and H. H. Hu, 2004: *Fluid Mechanics*. 3rd ed. Elsevier, 759 pp.
- Kutsuwada, K., M. Koyama, and N. Morimoto, 2009: Validation of gridded surface wind products using spaceborne microwave sensors and their application to air-sea interaction in the Kuroshio Extension region. *J. Remote Sens. Soc. Japan*, **29**, 179–190, doi:10.11440/rssj.29.179.
- Lozovatsky, I., M. Figueroa, E. Roget, H. J. S. Fernando, and S. Shapovalov, 2005: Observations and scaling of the upper mixed layer depth in the North Atlantic. *J. Geophys. Res.*, **110**, C05013, doi:10.1029/2004JC002708.
- Marshall, J. C., A. J. G. Nurser, and R. G. Williams, 1993: Inferring the subduction rate and period over the North Atlantic. *J. Phys. Oceanogr.*, **23**, 1315–1329, doi:10.1175/1520-0485(1993)023<1315:ITSRAP>2.0.CO;2.
- Monin, A. S., and A. M. Obukhov, 1954: Basic laws of turbulent mixing in the surface layer of the atmosphere. *Tr. Akad. Nauk SSSR Geofiz. Inst.*, **24**, 163–187.
- Obata, A., J. Ishizaka, and M. Endoh, 1996: Global verification of critical depth theory for phytoplankton bloom with climatological in situ temperature and satellite ocean color data. *J. Geophys. Res.*, **101**, 20 657–20 667, doi:10.1029/96JC01734.
- Pollard, R. T., P. B. Rhines, and R. O. R. Y. Thompson, 1973: The deepening of the wind-mixed layer. *Geophys. Fluid Dyn.*, **4**, 381–404, doi:10.1080/0309197208236105.
- Qiu, B., and K. A. Kelly, 1993: Upper-ocean heat balance in the Kuroshio Extension region. *J. Phys. Oceanogr.*, **23**, 2027–2041, doi:10.1175/1520-0485(1993)023<2027:UOHBIT>2.0.CO;2.
- Rossby, C. G., and R. B. Montgomery, 1935: *The Layer of Frictional Influence in Wind and Ocean Currents*. Vol. 3. Massachusetts Institute of Technology and Woods Hole Oceanographic Institution, 101 pp.
- Sverdrup, H. U., 1953: On conditions for the vernal blooming of phytoplankton. *J. Cons. Int. Explor. Mer*, **18**, 287–295, doi:10.1093/icesjms/18.3.287.
- Tomita, H., M. Kubota, M. F. Cronin, S. Imawaki, M. Konda, and H. Ichikawa, 2010: An assessment of surface heat fluxes from J-OFURO2 at the KEO and JKEO sites. *J. Geophys. Res.*, **115**, C03018, doi:10.1029/2009JC005545.
- Yoshikawa, Y., K. Akitomo, and T. Awaji, 2001: Formation process of intermediate water in baroclinic current under cooling. *J. Geophys. Res.*, **106**, 1033–1051, doi:10.1029/2000JC000226.
- , T. Matsuno, K. Marubayashi, and K. Fukudome, 2007: A surface velocity spiral observed with ADCP and HF radar in the Tsushima Strait. *J. Geophys. Res.*, **112**, C06022, doi:10.1029/2006JC003625.
- , T. Endoh, T. Matsuno, T. Wagawa, E. Tsutsumi, H. Yoshimura, and Y. Morii, 2010: Turbulent bottom Ekman boundary layer measured over a continental shelf. *Geophys. Res. Lett.*, **37**, L15605, doi:10.1029/2010GL044156.
- , C. M. Lee, and L. N. Thomas, 2012: The subpolar front of the Japan/East Sea. Part III: Competing roles of frontal dynamics and atmospheric forcing in driving ageostrophic vertical circulation and subduction. *J. Phys. Oceanogr.*, **42**, 991–1011, doi:10.1175/JPO-D-11-0154.1.
- Zikanov, O., D. Slinn, and M. Dhanak, 2003: Large-eddy simulations of the wind-induced turbulent Ekman layer. *J. Fluid Mech.*, **495**, 343–368, doi:10.1017/S0022112003006244.
- Zilitinkevich, S., 1972: On the determination of the height of the Ekman boundary layer. *Bound.-Layer Meteor.*, **3**, 141–145, doi:10.1007/BF02033914.
- , A. Baklanov, J. Rost, A.-S. Smedman, V. Lykosov, and P. Calanca, 2002: Diagnostic and prognostic equations for the depth of the stably stratified Ekman boundary layer. *Quart. J. Roy. Meteor. Soc.*, **128**, 25–46, doi:10.1256/00359000260498770.
- , I. Esau, and A. Baklanov, 2007: Further comments on the equilibrium height of neutral and stable planetary boundary layers. *Quart. J. Roy. Meteor. Soc.*, **133**, 265–271, doi:10.1002/qj.27.